PHYSICS

Direct imaging of ultrafast lattice dynamics

S. Brennan Brown[1]*, A. E. Gleason[2,3], E. Galtier[4], A. Higginbotham[5], B. Arnold[4], A. Fry[4], E. Granados[4], A. Hashim[6], C. G. Schroer[7,8], A. Schropp[7], F. Seiboth[4,7], F. Tavella[4], Z. Xing[4], W. Mao[3,9], H. J. Lee[4], B. Nagler[4]

Under rapid high-temperature, high-pressure loading, lattices exhibit complex elastic-inelastic responses. The dynamics of these responses are challenging to measure experimentally because of high sample density and extremely small relevant spatial and temporal scales. Here, we use an x-ray free-electron laser providing simultaneous in situ direct imaging and x-ray diffraction to spatially resolve lattice dynamics of silicon under high–strain rate conditions. We present the first imaging of a new intermediate elastic feature modulating compression along the axis of applied stress, and we identify the structure, compression, and density behind each observed wave. The ultrafast probe x-rays enabled time-resolved characterization of the intermediate elastic feature, which is leveraged to constrain kinetic inhibition of the phase transformation between 2 and 4 ns. These results not only address long-standing questions about the response of silicon under extreme environments but also demonstrate the potential for ultrafast direct measurements to illuminate new lattice dynamics.

INTRODUCTION

Understanding the processes by which crystalline solids react to rapid compression and heating is an interdisciplinary endeavor spanning geophysics (1), high energy density sciences (2), and materials engineering (3). When subjected to shock loading, the strong interatomic bonds of solid materials—metals, minerals, ceramics, and semiconductors—result in a lattice response with both elastic (compression with no structural changes) and inelastic (lattice rearrangement and disassembly) components (4). Insight into the kinetics and interplay of these processes is of key importance for understanding damage mechanisms and formation of new compounds. Driven by high-power lasers capable of compressing solids to high-pressure states, recent experiments probed the inelastic response of solids into twinned lattices, high-pressure phases, and melt (5–9). Measuring the kinetics of these responses is challenging, as shocks develop over nanosecond time scales and short probe attenuation lengths in solids often frustrate direct measurements (4, 10).

In this work, we use an ultrafast x-ray free-electron laser to perform simultaneous in situ x-ray diffraction and x-ray phase-contrast imaging of shock-compressed silicon, enabling direct probing of the combined elastic-inelastic response with subnanosecond temporal resolution (11). Silicon was selected as a sample material in this study because, despite an extensive body of experimental literature, lively debate regarding the nature of the elastic and inelastic shock responses (12–18) remains. Molecular dynamics and plasticity simulations predict an inelastic phase transition, but it is only within the past year that experiments have resolved the high-pressure crystalline structures necessary to refine computational models (19, 20). In addition, recent Laue diffraction experiments showed an anomalous elastic response with two distinct

compression regions, but as the response was not spatially resolved, the geometry and mechanism of the two elastic regions remained elusive (21, 22). Simulations suggest that the material may exhibit a dual-elastic plateau following the primary elastic wave along the shock direction (23).

This study captures the first experimental imaging of multiple transient elastic regimes, characterizes the crystalline structure of each progressive shock wave, and uses the unique high coherence of the Linac Coherent Light Source (LCLS) to extract the compression across both elastic features in situ. The data provide evidence of a primary elastic wave of compression exceeding the expected Hugoniot elastic limit (HEL) from gas-gun experiments, a new intermediate elastic wave that modulates sample stress back toward the HEL, a high-pressure phase transition, and subsequent melt. We connect observed propagation of the intermediate elastic wave to kinetics of the high-pressure phase transformation, constraining onset between 2 and 4 ns after shock incidence. These results present a spatially resolved analysis of an elastic-inelastic response under high–strain rate conditions and provide experimental evidence of new ultrafast lattice reactions over small temporal and spatial scales. Combining simultaneous direct visualization and structure determination of lattice dynamics represents a meaningful step forward in understanding how crystalline materials react to rapid loading and opens the doors to discoveries of new transient structures and mechanisms.

RESULTS

Shock-compressed matter

Figure 1 shows the target construction and experimental geometry. To drive a shockwave through the silicon sample, a high-power optical laser (λ = 527 nm) at the Matter in Extreme Conditions (MEC) endstation of the LCLS ablated 25 μm of plastic from the front of the target (24). A leading layer of 200-nm aluminum flash coating on the plastic ablator increased energy absorption (25). Each optical drive pulse had a temporal profile that rose to 7.5×10^{11} W/cm^2 within 1 ns and increased linearly to 2.5×10^{12} W/cm^2 by the end of the 15-ns pulse duration.

To measure the evolving atomic dynamics of silicon under shock-wave compression, a single x-ray pulse from the LCLS passed through the sample perpendicular to the high-power optical laser drive beam. A series of beryllium-focusing lenses brought the x-ray bunch to its

[1]Department of Mechanical Engineering, Stanford University, Building 530, 440 Escondido Mall, Stanford, CA 94305, USA. [2]Shock and Detonation Physics, Los Alamos National Laboratory, P.O. Box 1663, Los Alamos, NM 87545, USA. [3]Stanford Institute for Materials and Energy Sciences, SLAC National Accelerator Laboratory, 2575 Sand Hill Rd., Menlo Park, CA 94025, USA. [4]Linac Coherent Light Source, SLAC National Accelerator Laboratory, 2575 Sand Hill Rd., Menlo Park, CA 94025, USA. [5]York Plasma Institute, Department of Physics, University of York, Heslington, YO10 5DD, UK. [6]Department of Physics, University of California, Berkeley, Berkeley, CA 94720, USA. [7]Photon Science, Deutsches Elektronen-Synchrotron DESY, Notkestrasse 85, D-22607 Hamburg, Germany. [8]Department Physik, Universität Hamburg, Luruper Chaussee 149, 22761 Hamburg, Germany. [9]Department of Geological Sciences, Stanford University, 367 Panama St., Stanford, CA 94305-2220, USA.
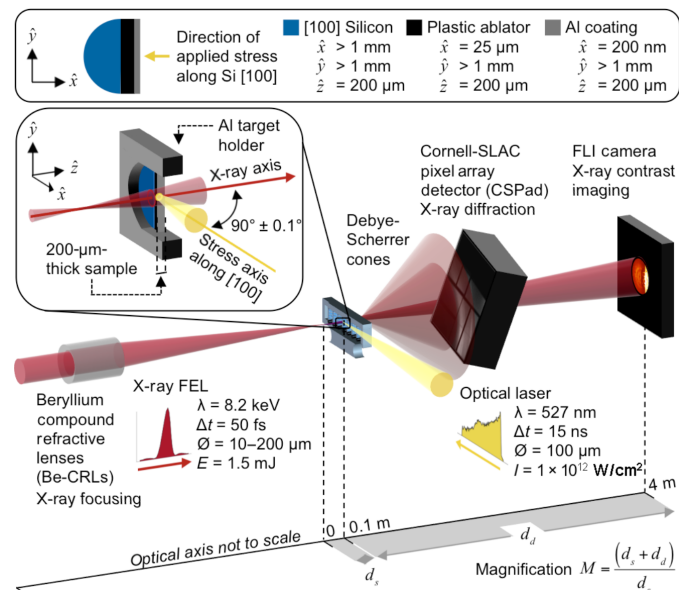*Corresponding author. Email: sbbrown@slac.stanford.edu

Fig. 1. Experimental configuration of optical drive laser and probe x-ray free-electron laser. X-ray diffraction captured the lattice response of shocked silicon, showing dynamics of high-pressure phases and melt. X-ray phase-contrast imaging provided direct snapshots of shock propagation in the target and revealed elastic features. These simultaneous, ultrafast measurements allowed resolution of silicon crystalline phases, compression, and density before and after multiple shock features. Upper inset: Unshocked target construction with the shock direction (direction of applied stress) perpendicular (transverse) to the imaging x-ray axis. FLI, Finger Lakes Instrumentation; FEL, free-electron laser.

tightest focus 10 cm before the target surface; consequently, the x-rays diverged before hitting the sample, and the resulting x-ray field-of-view on-target was adjustable between 10 and 200 μm in diameter. Keeping the 10-μm field-of-view probe x-ray fixed in space and moving the target holder enabled selective probing before and after shock features. Diffraction of the 50-fs ultrabright probe x-ray was captured on Cornell–SLAC pixel array detectors (CSPads) provided by MEC. The undiffracted photons in the x-ray pulse continued to the phase-contrast imaging instrument located 4 m from the target interaction point. By placing the imaging detector far downstream, the divergence of the x-ray pulse magnified imaged features, enabling submicrometer resolution (26). Phase-contrast imaging measured the compression across the elastic shock features, which converts to stress using nonlinear material elastic relations (see the "Experimental design" and "X-ray phase-contrast imaging" sections in Materials and Methods).

X-ray diffraction

Figure 2 shows in situ phase-contrast images and x-ray diffraction data from six shots taken at the same time delay and optical drive laser intensity (see the "Experimental design" section in Materials and Methods). At the top of both diagrams, the initial shot (whole shock) was recorded using a 200-μm x-ray field of view. The diffraction shows multiple broad peaks and the first silicon melt feature located between 2.8 and 3.25 Å^{-1} (27, 28). The phase-contrast image reveals a multiple-shockwave elastic-inelastic lattice response with a resolution of approximately 5 μm.

A spatial scan of 10-μm x-ray field-of-view shots progresses from left to right along the bottom of Fig. 2A. As illustrated in Fig. 2B, diffraction from first and second spatial shots shows no strong peaks in the az-

imuthally integrated data, indicating that the sample path remained in the ambient cubic diamond phase. Diffraction from location 3 shows broad peaks corresponding to overlapping d-spacing of the Si-II (I4$_1$/amd similar to β-Sn), Si-XI (Imma), and Si-V (P6/mmm similar to simple hexagonal) high-pressure phases. This overlap suggests the progression of several high-pressure structures along the transverse x-ray path, as Si-XI is a structural intermediate between Si-II and Si-V. The two-dimensional (2D) diffraction data displayed a preferred crystalline orientation with intense single-crystal spots in the polycrystalline bands, matching well with the recent x-ray diffraction experiments (18). Last, spatial locations 4 and 5 show an increasingly strong diffuse feature in their diffraction and a decrease in x-ray transmission through the sample. As the environment lies along the high-pressure, high-temperature principal Hugoniot, this is attributed to shock-induced melting.

X-ray phase-contrast imaging

Elastic shocks are sharp discontinuities in the sample density, and the probe x-rays see these features as a change in the material index of refraction. Traversing these elastic features introduces a change in phase in the coherent x-ray bunch, which, when propagated 4 m downstream, manifests as a fringe shift visible on the phase-contrast imaging detector. Using the lineout of phase-contrast data in Fig. 3A, the visibility, phase shift, and change in density across the elastic features can be determined (see the "X-ray phase-contrast imaging" section in Materials and Methods) (29). From the data in Fig. 3A, the compression across the first elastic feature (hereafter referred to as "E1") is 14%. The second elastic feature (hereafter referred to as "E2") has a smaller visibility with an absolute decrease in compression across the feature of 3%. The strength of E2 subsided away from the central line of applied stress, disappearing at the edge of the 200-μm x-ray field of view. To confirm the number of x-ray phase rotations through the material, sign of phase rotation (compression or tension), and corresponding density values, a forward simulation propagated a coherent beam with the calculated phase shifts at each elastic feature location and recreated the lineout pattern (see the "Simulation" section in Materials and Methods).

Figure 3B shows five spatially integrated lineouts from a temporal scan of shots. Accounting for the 25-μm plastic ablator at each time step, E1 has a speed of 10.0 ± 2 km/s, a value consistent with previously reported literature values for the primary elastic shock (12, 17). E1 is also the strongest feature, although its strength decreases with time; this decrease in elastic shock strength aligns with literature observations (17). After 4 ns, E2 becomes visible via phase-contrast imaging. The upper inset of Fig. 3B graphs the calculated values of compression behind the two elastic features at several time delays. The compression plotted is the volumetric change in density across the feature. The compression across E1 ranges between 13 and 16%, and the difference in density across E2 ranges between 2 and 4% as the features propagate. Normalizing by shock rise time, the average strain rate can be characterized as "extremely high" (17).

DISCUSSION

The data presented in Figs. 2 and 3 address long-standing uncertainty about the elastic-inelastic response of silicon under high–strain rate shock conditions. Under the specified drive parameters, [100] silicon exhibits a primary elastic shockwave (E1), a secondary elastic feature (E2), an inelastic phase transition, and melt. Figure 2A images these
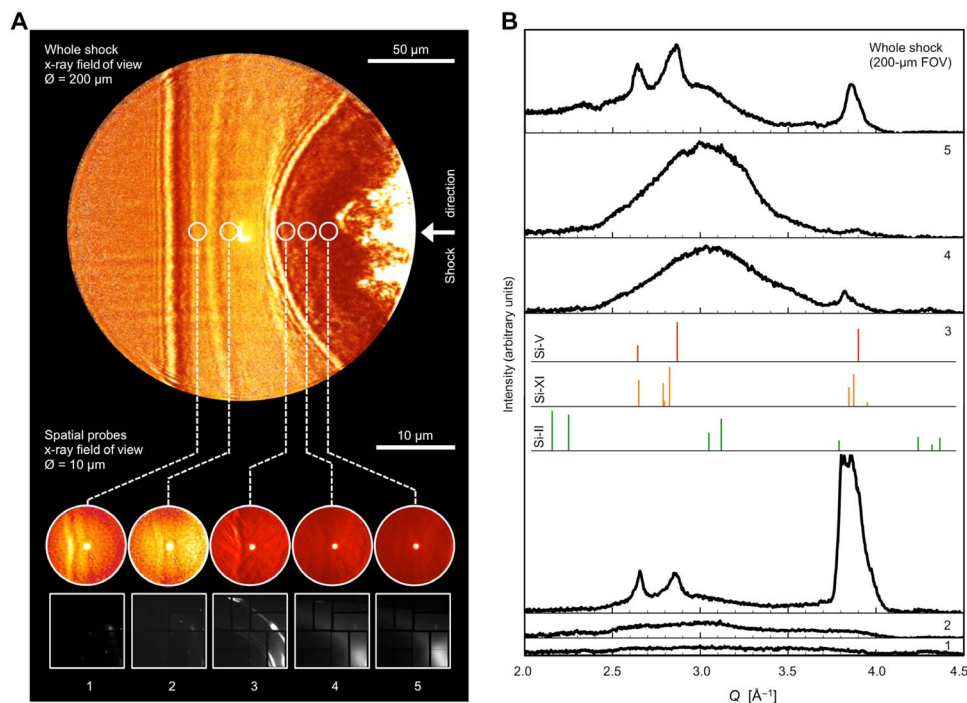
Fig. 2. X-ray data taken at a 15-ns time delay. (**A**) Phase-contrast images of the 200-μm field-of-view "whole shock" and 10-μm field-of-view spatial scan, revealing a multiple-shockwave structure. On the basis of x-ray diffraction, the first two features (positions 1 and 2) remain in the ambient cubic diamond phase, the third feature is in an inelastic phase transition (position 3), and the sample shows evidence of melt further to the right (positions 4 and 5). Spatial probe placement is accurate within 5 μm. Spatial probes (10-μm field of view) are taken at the following positions from the laser-incident edge of the silicon [100] target in the direction of applied stress: position 1, 125 μm; position 2, 105 μm; position 3, 75 μm; position 4, 62 μm; position 5, 50 μm. (**B**) Azimuthally integrated x-ray diffraction from a 200-μm x-ray field-of-view (FOV) shot of whole shock and five 10-μm x-ray field-of-view spatial scan shots. Colored lines denote expected locations of silicon high-pressure peaks for relevant phases. Traces are offset to facilitate viewing, but intensity values remain unaltered.

regimes occurring simultaneously in a single sample under dynamic compression.

The primary elastic shockwave (E1) typically represents compression to a material's HEL. Substituting the macroscopic strain values found via phase-contrast imaging across E1 into nonlinear elastic relation for silicon in the [100] direction given by Eq. 1 provides an estimate of the difference in longitudinal stress across the feature (14, 30).

$$\sigma_x = 165.77\mu - 1.93\mu^2 (GPa) \qquad (1)$$

where μ is the macroscopic strain

$$\mu = \frac{\rho}{\rho_0} - 1 \qquad (2)$$

For the macroscopic strains given in Fig. 3B, the corresponding stresses σ_x along the primary shock direction range between 21 and 26 GPa. As the HEL for silicon [100] occurs at approximately 11 GPa in previous works, this indicates that the shock system is strongly overcompressed (12, 13, 15, 19). Knowing the density of the original, unshocked silicon $\rho = 2.33$ g/cm^3 and the 13 to 16% change in compression calculated via phase-contrast imaging determines that the density rises to $\rho = 2.65$ to 2.7 g/cm^3 after E1.

The secondary elastic feature (E2) becomes visible after 4 ns. The visibility of E2 is strongest in the central regions of the optical laser drive, suggesting that the volume collapse of the phase transition wave affects

its generation and propagation. While the calculated longitudinal stress drop across E2 is between 3 and 6 GPa, phase-contrast imaging does not assume uniform compression between the two elastic features; consequently, the absolute value of the density after E2 falls within a range of values. Figure 4 plots the calculated densities of these regions with unknown gradients represented by gray dashed lines and gray error bars. Additional diffraction data taken with a 10-μm x-ray field of view directly before the inelastic wave show the Si-I compressed by only 5%. When input to the nonlinear elastic relation, this compression yields a longitudinal stress of 9 ± 2 GPa, indicating that the sample is modulated back toward the expected HEL after E2. This dual elastic plateau of E1 and E2 is the first direct imaging of features predicted by recent elasticity and molecular dynamics simulations of laser-driven shocked silicon, and the elastic macroscopic compressions predicted by simulation and observed in previous Laue diffraction measurements match well with the compressions reported in this study (19, 21–23).

Multiple sources support the notion that changes in elastic stress are mediated by an inelastic mechanism in silicon. Molecular dynamics calculations predicted that ambient silicon transforms to Si-XI in a banded structure, and several experiments observed evidence of transitions to Si-II, Si-V, and amorphous phases (15, 18–20, 31). Experimental x-ray diffraction determination of the nonelastic mechanism is complicated by a variation in drive parameters and a high mosaic spread from the inelastic region (21, 23). The diffraction from Fig. 2B unambiguously attributes the structural volume collapse mechanism to a high-pressure inelastic phase transition wave and subsequent melt. Analysis of the Si-V diffraction peaks indicates that the pressure within the inelastic
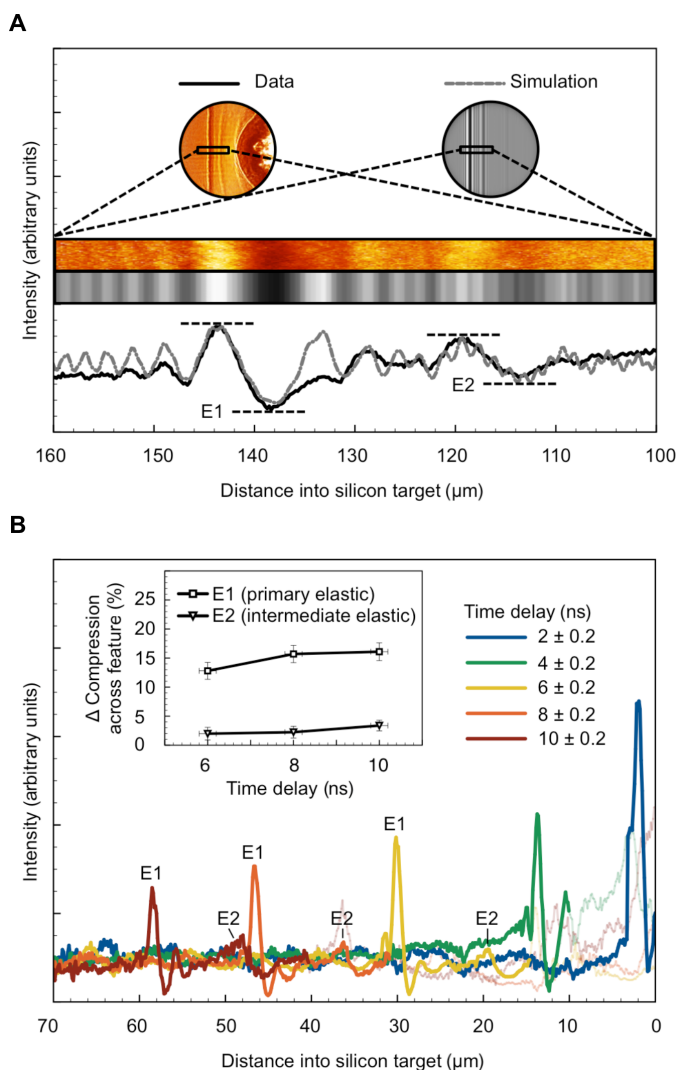
Fig. 3. Phase-contrast imaging. (**A**) Intensity lineouts from the phase-contrast imaging data and a forward simulation of phase changes observed across the elastic features. The discrepancy between simulated and observed intensity values at spatial location 135 μm into the target likely emerges as the simulation does not assume any specific shock width or gradient between the two elastic features. (**B**) Intensity lineouts from imaging at increasing time delays between shock incidence and probe x-ray. An inset graphs the calculated compressions across each elastic feature at increasing time delays. Compression values are only shown for 6-, 8-, and 10-ns delays as the secondary elastic feature only becomes visible at 4 ns.

Fig. 4. Shockwave characterization. The bottom image maps the silicon [100] shockwave structure spatially, and black lines mark the densities calculated via phase-contrast imaging and x-ray diffraction. The calculated compression of 14% across E1 takes the unshocked silicon density of 2.33 to 2.65 g/cm³. As the density slope between E1 and E2 is not known, gray dashed lines show the range of potential density values. X-ray diffraction shows evidence of several high-pressure phases of silicon; their densities are mapped in an increasing order. As the sample melts, diffuse scatter overwhelms the x-ray diffraction signal. Silicon structures are reproduced using VESTA (38–40).

wave is 21 ± 2 GPa, which falls within the range of stresses calculated at the overcompressed primary elastic wave via phase-contrast imaging (32). Existence of multiple high-pressure silicon phases over the 50-fs probe x-ray path is supported by Tsujino *et al.*'s (33) recovery experiments that used transmission electron microscopy and grazing-incidence x-ray diffraction to identify Si-II, Si-XI, and Si-V coexisting in a single recovered sample after irradiation with a femtosecond optical drive laser.

The experimental complexity of measuring lattice dynamics under laser-driven shock compression introduces several sources of error. First, in the transverse configuration shown in Fig. 1, the x-ray pulses probe through a 3D shock, integrating structure and density informa-
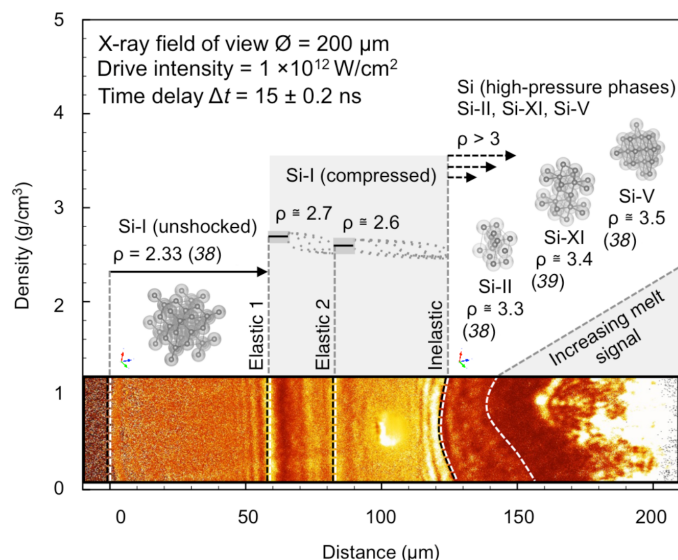
tion along their measurement path. This geometrical consideration explains the broad high-pressure phase diffraction in Fig. 2B; even when focused to a 10-μm x-ray field of view to minimize sampling gradients in $\hat{x}$, the incident x-rays yield information about a variety of stress states radiating out from the central axis of applied stress in $\hat{z}$. Second, the coverage of the x-ray detector provides insufficient q range to make a definitive high-pressure phase determination or resolve the second silicon melt feature at >5 Å⁻¹ (27, 28). Thus, only qualitative conclusions affirming the appearance of both high-pressure phase transformation and subsequent melt can be made. Last, because of both the highly transient nature of the feature and the relatively small absolute change in compression across it, traditional rear-surface interferometry struggles to resolve the intermediate elastic wave. Consequently, we use direct imaging to extract system information such as wave speed.

Figure 4 summarizes the results of combined x-ray diffraction and x-ray phase-contrast measurements, plotting the calculated density across the multiple shockwave structure and assigning a crystalline structure to each region. In addition to this spatially resolved characterization of the shock response in silicon, this work contains two broader takeaways. First, solid lattices can sustain stresses greater than their expected HEL for nanosecond time scales until inelastic deformation can occur. This phenomenon has been observed on picosecond time scales in shocked copper; silicon preserves the overcompressed state three orders of magnitude longer (8). Once a high-pressure phase transition initiates, its inherent volume collapse can pull back on the overcompressed lattice, creating the intermediate elastic feature that modulates the sample back toward the HEL. Second, the high-pressure phase transition is kinetically inhibited for 2 to 4 ns under these shock conditions. At 2 ns, there is neither evidence of E2 in the phase-contrast imaging nor polycrystalline bands from high-pressure phases in the
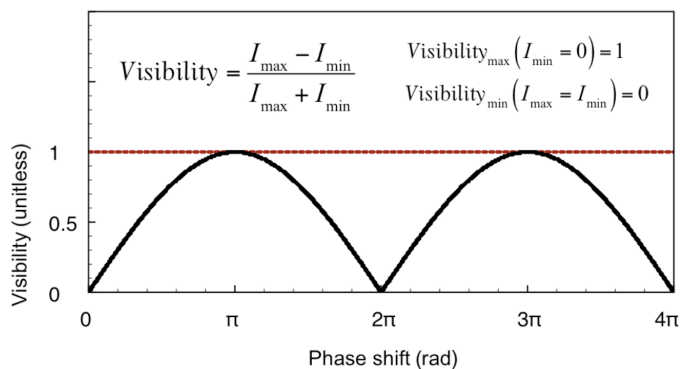
$$Visibility = \frac{I_{max} - I_{min}}{I_{max} + I_{min}} \qquad Visibility_{max}(I_{min}=0) = 1$$
$$Visibility_{min}(I_{max}=I_{min}) = 0$$

Fig. 5. Relation between visibility and phase. This visibility corresponds to a change in phase induced in the propagated electromagnetic wave as it passes through a density discontinuity in the material. The red dashed line shows the maximum visibility.

diffraction data. However, both appear in data taken at 4 ns. Using an experimental fit of the E2 wave speeds from Fig. 3B to calculate when E2 first forms can further constrain this kinetic window to between 2 and 3 ns. This response time scale is a key input when calculating the reaction rate constant and enthalpy barriers for inelastic phase transitions. A 2-ns phase transition rate supports previous simulation work estimating that the enthalpy barrier necessary for silicon to transition from its ambient cubic diamond structure to Si-II ($I4_1/amd$ similar to β-Sn) falls on the order of 100 meV (34).

In summary, this study combines direct imaging and x-ray diffraction to spatially resolve the lattice structure and dynamics of silicon under high–strain rate conditions. Observation of the transient intermediate elastic wave addresses the anomalous elastic behavior of silicon seen in recent works and supports a dual-elastic plateau predicted by simulations. The ultrafast nature of the probe x-rays enables time-resolved propagation of the intermediate elastic feature, which is leveraged to uniquely constrain the kinetic inhibition of the inelastic phase transformation. This work required pushing the LCLS to its current operational limits; without the ultrabright, highly coherent hard x-rays capable of producing phase-contrast fringes through a dense solid, quantification of the ultrafast elastic feature would not have been possible. Future investigations can not only build upon the mechanisms and kinetics of the observed transient interactions in this work but also extend the methodology to study other materials under extreme conditions. The ability to simultaneously directly image and characterize the crystalline structures of a system with high temporal and spatial resolution markedly improves understanding of high–strain rate phenomena and enables discovery of new, transient lattice responses.

MATERIALS AND METHODS
Experimental design
To drive shockwaves through the material, the MEC endstation of the LCLS at the SLAC National Accelerator Laboratory provided a laser (2.0 J, λ = 527 nm) focused to a 100-μm-diameter on-target normal (35). To create a "top hat" spatial profile, the optical laser passed through a phase plate and generated an average intensity of 1×10^{12} W/cm^2. The drive temporal profile was selected to maintain pressure as a function of time (35). The target construction along the shockwave ($\hat{x}$) axis consisted of [100] silicon with an aluminum

flash–coated plastic ablator affixed. The optical drive laser ablated the flash-coated plastic, sending a shockwave into the attached silicon. The shock propagation speed was measured via direct imaging, and the calculated velocity could be transformed to pressure using documented shock Hugoniot data to check longitudinal stress values calculated via phase-contrast imaging and the nonlinear elastic relations (35, 36). Initially determined by the diameter of the optical laser on-target, the spatial size of the inelastic shock front grew as it propagated through the silicon target. The spatial profile of the primary elastic shock front remained linear and uniform at all time delays because of the 1-mm halo of optical drive laser light created by the phase plate element pattern. While this light was low in intensity, the primary elastic wave in silicon is relatively insensitive to pressure below the HEL and thus appears in all shots presented herein. Probe times were informed by phase-contrast images to determine when the shock front had not yet reached the sample dimensions and when the environment could be classified as free from significant edge effects.

To measure evolving atomic structure of silicon during laser-driven shockwave compression and provide direct imaging, the LCLS delivered a 50-fs pulse of 8.2 keV, fully transverse coherent x-rays with a bandwidth of $\Delta E/E = 0.1\%$. The angle between the optical drive laser and the probe x-rays was 90° ± 0.1°. The x-ray field-of-view on-target was adjusted by changing the distance between the target and a set of upstream focusing beryllium lenses set in point-source geometry. The x-ray bunch reached its tightest focus (200-nm diameter) 10 cm before the target surface. In this imaging configuration, the x-ray field of view is equal to the diameter of illumination provided by the focused x-rays on-target. The time delay between the optical drive and probe x-rays could be adjusted between −10 and +30 ns after the beginning of laser ablation (26). The time delay had a temporal jitter of 20 ps, and the pulse overlaps and profiles were recorded every shot on an oscilloscope trace.

The whole shock image in Fig. 2 was taken using a 100-μm-diameter optical drive laser with phase plate inserted and a 200-μm x-ray field of view. After optical laser and x-ray irradiation, each sample was destroyed; for every new shot, the sample holder was moved to position a fresh target at the x-ray and optical laser interaction point. The whole shock image was repeated >15 times on new samples to ensure reproducibility. The spatial scan in Fig. 2 was taken using the same optical drive laser parameters and a 10-μm x-ray field of view. Between each shot, the target holder was shifted to the desired spatial location, while all other parameters, including drive timing, remained constant. The temporal scan in Fig. 3B was taken with a 100-μm optical drive laser with phase plate inserted and 200 μm x-ray fields of view. Between each shot, a delay stage in the optical drive beam was adjusted to change the nanosecond timing.

X-ray diffraction
The CSPads collected data on a shot-by-shot basis with experiment-specific metrology and were positioned to cover a set range of 2θ diffraction angles from 18° to 70°. Before each driven shot, an x-ray–only shot was taken to provide backgrounds for the diffraction and phase-contrast instruments. The x-ray–only shots left no damage on the surface of the target visible via diagnostics. After reactivating the laser and taking the driven shot, the data were normalized by the x-ray–only values. This normalization resulted in the flat diffraction lineouts for probes through a material that remained in the ambient cubic diamond phase. On the x-ray diffraction CSPads, a mask was applied on the nonactive surface to reduce the background signal, although this had a small effect, particularly on the shots with melt and diffraction data.

The normalized and masked diffraction images were azimuthally integrated using Dioptas (37). The detector spatial calibration was performed using x-ray–only diffraction from a CeO_2 sample. Ambient condition diffraction spots from the aluminum target holder were masked to avoid confusion.

X-ray phase-contrast imaging

Data collected from the phase-contrast instrument was comparably normalized by respective x-ray–only shots, which mitigated propagated lens defects. In the center of each image, a bright spot appeared; this is the third harmonic of the x-ray free-electron laser, which focuses differently from the fundamental wavelength because of its higher photon energy. This feature is most obvious in Fig. 2 spatial scan images, as no x-ray–only background images were saved and were consequently not subtracted. These images were not used for any quantitative purposes. The phase-contrast images in Figs. 2 to 4 were processed with ImageJ to their current color scheme, but all quantitative data were collected with images processed only by the aforementioned x-ray–only normalization. The color scheme was applied evenly, without bias or alteration, to the entire data image.

To calculate the compression across the two elastic waves, the visibility of the two features was measured from their lineouts according to Eq. 3. V is the visibility, I_{max} is the maximum intensity, and I_{min} is the minimum intensity across a feature.

$$V = \frac{I_{max} - I_{min}}{I_{max} + I_{min}} \qquad (3)$$

Each value of visibility corresponds to a phase shift ($\Delta\phi$) created by infinitesimal changes in density over the elastic shocks. To quantify the relationship between phase shift and visibility, a simulation propagated an 8.2-keV probe x-ray beam with a specified phase shift. This was repeated across 10,000 shocks of increasing phase shift to create Fig. 5.

This change in density can be calculated by comparing the difference in x-ray path length (Δl) across each individual shock.

$$\Delta l = d[n_1 - n_2] \, (\text{meters}) \qquad (4)$$

n_1 and n_2 are the complex indices of refraction before and after the elastic shock, respectively, and d is the propagation distance. In this work, d is the thickness of the material along the propagation direction. A general complex index of reflection can be expressed as

$$n = 1 - \delta + i\beta \qquad (5)$$

where δ is the dispersive term and β is the absorptive term.

$$\delta = \frac{n_a r_e \lambda^2}{2\pi} f_1 \qquad (6)$$

$$\beta = \frac{n_a r_e \lambda^2}{2\pi} f_2 \qquad (7)$$

n_a is the number density of the material. r_e is the classical electron radius (2.8179×10^{-15} m). λ is the wavelength of the probe x-rays (1.5120×10^{-10} m for 8.2-keV radiation). f_1 and f_2 are the silicon atomic

scattering factors. $f_1 = 14.261519$ e/atom and $f_2 = 0.3190926$ e/atom at 8.2 keV.

Therefore, n_1 and n_2 across an elastic shock can be written as

$$n_1 = 1 - \delta_1 + i\beta_1 = 1 - \frac{n_{a1} r_e \lambda^2}{2\pi} f_1 + i \frac{n_{a1} r_e \lambda^2}{2\pi} f_2 \qquad (8)$$

$$n_2 = 1 - \delta_2 + i\beta_2 = 1 - \frac{n_{a2} r_e \lambda^2}{2\pi} f_1 + i \frac{n_{a2} r_e \lambda^2}{2\pi} f_2 \qquad (9)$$

Substituting n_1 and n_2 into the equation for x-ray path difference results in the following

$$\Delta l = d[n_1 - n_2] \qquad (10)$$

$$\Delta l = d[(1 - \delta_1 + i\beta_1) - (1 - \delta_2 + i\beta_2)] \qquad (11)$$

This simplifies to

$$\Delta l = d\left[\frac{r_e \lambda^2}{2\pi}\right][(n_{a2} - n_{a1})f_1 - i(n_{a2} - n_{a1})f_2] \qquad (12)$$

When solved for the difference in number density ($n_{a2} - n_{a1}$), this results in

$$(n_{a2} - n_{a1}) = \frac{\Delta l}{d\left[\frac{r_e \lambda^2}{2\pi}\right][f_1 - if_2]} \, (\text{atoms/m}^3) \qquad (13)$$

The difference in the optical path length can be calculated from the collected data by multiplying the determined phase shift across an elastic wave and multiplying it by the probe x-ray wavelength.

$$\Delta l = \frac{\lambda \Delta\phi}{2\pi} \qquad (14)$$

With the system fully constrained, the difference in the density and the corresponding compression of the material can be explicitly calculated. The minimum-resolvable change in phase with this experimental setup is approximately $2\pi/10$, indicating that a density change of 0.025 g/cm^3 in silicon will generate a phase-contrast fringe. For the data presented in Fig. 3A, the change in phase across the primary elastic feature (E1) lies between π and 2π; as the visibility decreases, the compression increases. The change in phase across the secondary elastic feature (E2) lies between zero and π; as the visibility increases, the compression increases.

Simulation

To confirm the measured visibility values extracted from data matched with the correct phase shift of x-rays, a forward simulation reproduced the lineout pattern across the elastic features. This numerical approach consisted of generating an initial intensity field of a Gaussian x-ray beam incident on-target, creating a phase map of identical matrix dimensions and introducing phase shifts at the spatial locations and strengths observed in the experiment. The square root of the intensity field was then multiplied by the phase map to create the initial electric

field matrix. This electric field was decomposed into its spectral components via Fourier transform. Next, the initial electric field was multiplied by the free-space propagator to simulate propagating the beam downstream to the detector, and the magnitude of the resulting propagated electric field was taken to find the simulated intensity recorded on the detector. A lineout of the simulated intensity can be compared to a lineout from the experimental data, as demonstrated in Fig. 3A. Using this simulation methodology, multiple values of the phase shifts at each elastic wave location can be iterated to determine the closest lineout fit to experimental data.

REFERENCES AND NOTES

1. A. E. Gleason, C. A. Bolme, H. J. Lee, B. Nagler, E. Galtier, D. Milathianaki, J. Hawreliak, R. G. Kraus, J. H. Eggert, D. E. Fratanduono, G. W. Collins, R. Sandberg, W. Yang, W. L. Mao, Ultrafast visualization of crystallization and grain growth in shock-compressed SiO₂. *Nat. Commun.* **6**, 8191 (2015).
2. D. Kraus, N. J. Hartley, S. Frydrych, A. K. Schuster, K. Rohatsch, M. Rödel, T. E. Cowan, S. Brown, E. Cunningham, T. van Driel, L. B. Fletcher, E. Galtier, E. J. Gamboa, A. Laso Garcia, D. O. Gericke, E. Granados, P. A. Heimann, H. J. Lee, M. J. MacDonald, A. J. MacKinnon, E. E. McBride, I. Nam, P. Neumayer, A. Pak, A. Pelka, I. Prencipe, A. Ravasio, R. Redmer, A. M. Saunders, M. Schölmerich, M. Schörner, P. Sun, S. J. Turner, A. Zettl, W. Falcone, S. H. Glenzer, T. Döppner, J. Vorberger, High-pressure chemistry of hydrocarbons relevant to planetary interiors and inertial confinement fusion. *Phys. Plasmas* **25**, 056313 (2018).
3. C. E. Wehrenberg, D. McGonegle, C. Bolme, A. Higginbotham, A. Lazicki, H. J. Lee, B. Nagler, H.-S. Park, B. A. Remington, R. E. Rudd, M. Sliwa, M. Suggit, D. Swift, F. Tavella, L. Zepeda-Ruiz, J. S. Wark, In situ x-ray diffraction measurement of shock-wave-driven twinning and lattice dynamics. *Nature* **550**, 496 (2017).
4. Y. P. Raizer, *Physics of Shock Waves and High-temperature Hydrodynamic Phenomena* (Courier Corporation, 2002), pp. 685–710.
5. A. E. Gleason, C. A. Bolme, H. J. Lee, B. Nagler, E. Galtier, R. G. Kraus, R. Sandberg, W. Yang, F. Langenhorst, W. L. Mao, Time-resolved diffraction of shock-released SiO₂ and diaplectic glass formation. *Nat. Commun.* **8**, 1481 (2017).
6. J. H. Eggert, D. G. Hicks, P. M. Celliers, D. K. Bradley, R. S. McWilliams, R. Jeanloz, J. E. Miller, T. R. Boehly, G. W. Collins, Melting temperature of diamond at ultrahigh pressure. *Nat. Phys.* **6**, 40–43 (2010).
7. B. J. Demaske, V. V. Zhakhovsky, N. Inogamov, I. I. Oleynik, Ultrashort shock waves in nickel induced by femtosecond laser pulses. *Phys. Rev. B* **87**, 054109 (2013).
8. D. Milathianaki, S. Boutet, G. J. Williams, A. Higginbotham, D. Ratner, A. E. Gleason, M. Messerschmidt, M. M. Seibert, D. C. Swift, P. Hering, J. Robinson, W. E. White, J. S. Wark, Femtosecond visualization of lattice dynamics in shock-compressed matter. *Science* **342**, 220–223 (2013).
9. R. Briggs, M. G. Gorman, A. L. Coleman, R. S. McWilliams, E. E. McBride, D. McGonegle, J. S. Wark, L. Peacock, S. Rothman, S. G. Macleod, C. A. Bolme, A. E. Gleason, G. W. Collins, J. H. Eggert, D. E. Fratanduono, R. F. Smith, E. Galtier, E. Granados, H. J. Lee, B. Nagler, I. Nam, Z. Xing, M. I. McMahon, Ultrafast x-ray diffraction studies of the phase transitions and equation of state of scandium shock compressed to 82 GPa. *Phys. Rev. Lett.* **118**, 025501 (2017).
10. B. L. Henke, E. M. Gullikson, J. C. Davis, X-ray interactions: Photoabsorption, scattering, transmission, and reflection at E = 50-30000 eV, Z = 1-92. *Atom. Data Nucl. Data Tab.* **54**, 181–342 (1993).
11. P. Emma, R. Akre, J. Arthur, R. Bionta, C. Bostedt, J. Bozek, A. Brachmann, P. Bucksbaum, R. Coffee, F.-J. Decker, Y. Ding, D. Dowell, S. Edstrom, A. Fisher, J. Frisch, S. Gilevich, J. Hastings, G. Hays, P. Hering, Z. Huang, R. Iverson, H. Loos, M. Messerschmidt, A. Miahnahri, S. Moeller, H.-D. Nuhn, G. Pile, D. Ratner, J. Rzepiela, D. Schultz, T. Smith, P. Stefan, H. Tompkins, J. Turner, J. Welch, W. White, J. Wu, G. Yocky, J. Galayda, First lasing and operation of an ångstrom-wavelength free-electron laser. *Nat. Photonics* **4**, 641–647 (2010).
12. W. H. Gust, E. B. Royce, Axial yield strengths and two successive phase transition stresses for crystalline silicon. *J. Appl. Phys.* **42**, 1897 (1971).
13. T. Goto, T. Sato, Y. Syono, Reduction of shear strength and phase-transition in shock-loaded silicon. *Jpn. J. Appl. Phys.* **21**, L369 (1982).
14. S. J. Turneaure, Y. M. Gupta, X-ray diffraction and continuum measurements in silicon crystals shocked below the elastic limit. *Appl. Phys. Lett.* **90**, 051905 (2007).
15. S. J. Turneaure, Y. M. Gupta, Inelastic deformation and phase transformation of shock compressed silicon single crystals. *Appl. Phys. Lett.* **91**, 201913 (2007).
16. S. J. Turneaure, Y. M. Gupta, Real-time x-ray diffraction at the impact surface of shocked crystals. *J. Appl. Phys.* **111**, 026101 (2012).
17. R. F. Smith, R. W. Minich, R. E. Rudd, J. H. Eggert, C. A. Bolme, S. L. Brygoo, A. M. Jones, G. W. Collins, Orientation and rate dependence in high strain-rate compression of single-crystal silicon. *Phys. Rev. B* **86**, 245204 (2012).
18. S. J. Turneaure, N. Sinclair, Y. M. Gupta, Real-time examination of atomistic mechanisms during shock-induced structural transformation in silicon. *Phys. Rev. Lett.* **117**, 045502 (2016).
19. G. Mogni, A. Higginbotham, K. Gáal-Nagy, N. Park, J. S. Wark, Molecular dynamics simulations of shock-compressed single-crystal silicon. *Phys. Rev. B* **89**, 064104 (2014).
20. E. E. McBride, A. Krygier, A. Ehnes, E. Galtier, M. Harmand, Z. Konôpková, H. J. Lee, H.-P. Liermann, B. Nagler, A. Pelka, M. Rödel, A. Schropp, R. F. Smith, C. Spindloe, D. Swift, F. Tavella, S. Toleikis, T. Tschentscher, J. S. Wark, A. Higginbotham, Phase transition lowering in dynamically compressed silicon. *Nat. Phys.* **15**, 89–94 (2019).
21. A. Loveridge-Smith, A. Allen, J. Belak, T. Boehly, A. Hauer, B. Holian, D. Kalantar, G. Kyrala, R. W. Lee, P. Lomdahl, M. A. Meyers, D. Paisley, S. Pollaine, B. Remington, D. C. Swift, S. Weber, J. S. Wark, Anomalous elastic response of silicon to uniaxial shock compression on nanosecond time scales. *Phys. Rev. Lett.* **86**, 2349–2352 (2001).
22. S. Patel, M. J. Suggit, P. G. Stubley, J. A. Hawreliak, O. Ciricosta, A. J. Comley, G. W. Collins, J. H. Eggert, J. M. Foster, J. S. Wark, A. Higginbotham, Single hit energy-resolved Laue diffraction. *Rev. Sci. Instrum.* **86**, 053908 (2015).
23. A. Higginbotham, P. G. Stubley, A. J. Comley, J. H. Eggert, J. M. Foster, D. H. Kalantar, D. McGonegle, S. Patel, L. J. Peacock, S. D. Rothman, R. F. Smith, M. J. Suggit, J. S. Wark, Inelastic response of silicon to shock compression. *Sci. Rep.* **6**, 24211 (2016).
24. B. Nagler, B. Arnold, G. Bouchard, R. F. Boyce, R. M. Boyce, A. Callen, M. Campell, R. Curiel, E. Galtier, J. Garofoli, E. Granados, J. Hastings, G. Hays, P. Heimann, R. W. Lee, D. Milathianaki, L. Plummer, A. Schropp, A. Wallace, M. Welch, W. White, Z. Xing, J. Yin, J. Young, U. Zastrau, H. J. Lee, The matter in extreme conditions instrument at the Linac coherent light source. *J. Synchrotron Radiat.* **22**, 520–525 (2015).
25. J. S. Wark, R. R. Whitlock, A. Hauer, J. E. Swain, P. J. Solone, Shock launching in silicon studied with use of pulsed x-ray diffraction. *Phys. Rev. B* **35**, 9391(R) (1987).
26. B. Nagler, A. Schropp, E. C. Galtier, B. Arnold, S. B. Brown, A. Fry, A. Gleason, E. Granados, A. Hashim, J. B. Hastings, D. Samberg, F. Seiboth, F. Tavella, Z. Xing, H. J. Lee, C. G. Schroer, The phase-contrast imaging instrument at the matter in extreme conditions endstation at LCLS. *Rev. Sci. Instrum.* **87**, 103701 (2016).
27. N. Funamori, K. Tsuji, Pressure-induced structural change of liquid silicon. *Phys. Rev. Lett.* **88**, 255508 (2002).
28. F. H. Stillinger, T. A. Weber, Computer simulation of local order in condensed phases of silicon. *Phys. Rev. B* **31**, 5262 (1985).
29. A. Schropp, R. Hoppe, V. Meier, J. Patommel, F. Seiboth, Y. Ping, D. G. Hicks, M. A. Beckwith, G. W. Collins, A. Higginbotham, J. S. Wark, H. J. Lee, B. Nagler, E. C. Galtier, B. Arnold, U. Zastrau, J. B. Hastings, C. G. Schroer, Imaging shock waves in diamond with both high temporal and spatial resolution at an XFEL. *Sci. Rep.* **5**, 11089 (2015).
30. H. J. McSkimin, P. Andreatch Jr., Measurement of third-order moduli of silicon and germanium. *J. Appl. Phys.* **35**, 3312 (1964).
31. S. Zhao, E. N. Hahn, B. Kad, B. A. Remington, C. E. Wehrenberg, E. M. Bringa, M. A. Meyers, Amorphization and nanocrystallization of silicon under shock compression. *Acta Mater.* **103**, 519–533 (2016).
32. H. Olijnyk, S. K. Sikka, W. B. Holzapfel, Structural phase transitions in Si and Ge under pressures up to 50 GPa. *Phys. Rev. A* **103**, 137–140 (1984).
33. M. Tsujino, T. Sano, N. Ozaki, O. Sakata, M. Okoshi, N. Inoue, R. Kodama, A. Hirose, Quenching of high-pressure phases of silicon using femtosecond laser-driven shock wave. *Rev. Laser Eng.* **36**, 1218–1221 (2008).
34. K. Gáal-Nagy, D. Strauch, Transition pressures and enthalpy barriers for the cubic diamond→β-tin transition in Si and Ge under nonhydrostatic conditions. *Phys. Rev. B* **73**, 134101 (2006).
35. S. Brennan Brown, A. Hashim, A. Gleason, E. Galtier, I. Nam, Z. Xing, A. Fry, A. MacKinnon, B. Nagler, E. Granados, H. J. Lee, Shock drive capabilities of a 30-Joule laser at the matter in extreme conditions hutch of the Linac Coherent Light Source. *Rev. Sci. Instrum.* **88**, 105113 (2017).
36. S. P. Marsh, *LASL Shock Hugoniot Data* (University of California Press, 1980).
37. C. Prescher, V. B. Prakapenka, DIOPTAS: A program for reduction of two-dimensional x-ray diffraction data and data exploration. *High Press. Res.* **35**, 223–230 (2015).
38. J. Z. Hu, L. D. Merkle, C. S. Menoni, I. L. Spain, Crystal data for high-pressure phases of silicon. *Phys. Rev. B* **34**, 4679 (1986).
39. M. I. McMahon, R. J. Nelmes, New high-pressure phase of Si. *Phys. Rev. B* **47**, 8337(R) (1993).
40. K. Momma, F. Izumi, VESTA 3 for three-dimensional visualization of crystal, volumetric, and morphology data. *J. Appl. Crystallogr.* **44**, 1272–1276 (2011).

Citation: S. B. Brown, A. E. Gleason, E. Galtier, A. Higginbotham, B. Arnold, A. Fry, E. Granados, A. Hashim, C. G. Schroer, A. Schropp, F. Seiboth, F. Tavella, Z. Xing, W. Mao, H. J. Lee, B. Nagler, Direct imaging of ultrafast lattice dynamics. *Sci. Adv.* **5**, eaau8044 (2019).